ACCSCIENCE PUBLISHING

Materials Science in Additive Manufacturing

ORIGINAL RESEARCH ARTICLE

Explainable prediction of bead geometry in laser-arc hybrid additive manufacturing of Al–Cu alloy using a particle swarm optimization-based ensemble model

Runsheng Li[1], Hui Ma[1], Xingwang Bai[2], Boce Xue[1], Changze Li[1], Kui Zeng[1], Youheng Fu[3], Yonghui Liu[4]*, and Yanzhen Zhang[1]*

[1]College of Mechanical and Electronic Engineering, China University of Petroleum (East China), Qingdao, Shandong, China

[2]School of Mechanical Engineering, University of South China, Hengyang, Hunan, China

[3]School of Materials Science and Engineering, Huazhong University of Science and Technology, Wuhan, Hubei, China

[4]Shandong CharmRay Laser Technology Co., Ltd, Yantai, Shandong, China

Abstract

The weld bead is the basic structural unit in metal additive manufacturing, yet the multiphysics coupling inherent to hybrid laser-arc processing greatly complicates the prediction of bead dimensions. Despite the exploration of numerous predictive methods, research on explainable prediction of weld-bead dimensions remains limited. In this work, we developed a particle swarm optimization (PSO)-based ensemble prediction model (PSO-EP) for laser-arc hybrid additive manufacturing, and through SHapley Additive exPlanations (SHAP) analysis, comprehensively uncovered the underlying links between process variables and bead geometry. Experimental evidence indicated that our PSO-EP outperformed individual models and alternative ensembles, delivering superior accuracy, reflected by an R-squared value of 0.9567 for bead width and an R-squared value of 0.9492 for bead height, and markedly lowering prediction errors. The SHAP findings indicated that weld speed is the dominant determinant of bead width, while laser power plays a pivotal role in bead height. Subsequent single-factor dependence analysis showed that different process variables had significantly different impacts on bead size across their respective value intervals. This study provides important theoretical support for the intelligent development of the laser-arc hybrid additive manufacturing process.

Keywords: Additive manufacturing; Ensemble learning; Laser-arc hybrid; Geometry prediction; Aluminum–copper alloys; Explainable analysis

***Corresponding authors:**
Yonghui Liu
(78925411@qq.com)
Yanzhen Zhang
(zhangyanzhen@upc.edu.cn)

Citation: Li R, Ma H, Bai X, *et al*. Explainable prediction of bead geometry in laser-arc hybrid additive manufacturing of Al–Cu alloy using a particle swarm optimization-based ensemble model. *Mater Sci Add Manuf.* 2025;4(3):025220036.
doi: 10.36922/MSAM025220036

Received: May 26, 2025

Revised: June 16, 2025

Accepted: June 17, 2025

Published online: July 17, 2025

1. Introduction

Metal additive manufacturing (MAM), commonly referred to as metal 3D printing, is known for its design versatility and high efficiency, and is therefore extensively employed in aerospace, automotive, shipbuilding, and energy industries.[1] Through

the layer-by-layer deposition and solidification of metal feedstock, MAM creates new possibilities for designing and producing intricate metallic parts,[2-4] significantly enhances manufacturing productivity, propels innovation in product design and processing routes, and expedites the overall evolution of industrial manufacturing.[5,6] Among MAM technologies, powder bed fusion (PBF) and directed energy deposition (DED) are the most widespread;[7] wire-feed DED, in particular, garners interest for its superior deposition rates and material efficiency.[8,9] Wire-feed additive manufacturing utilizes lasers, electron beams, or welding arcs as energy inputs. In comparison with laser-or electron-beam-based AM, wire arc additive manufacturing (WAAM) offers significant benefits in capital expenditure and build rate.[10] The typical deposition rate for laser or electron beam AM lies between 2 and 10 g/min, whereas WAAM attains 50 – 130 g/min;[11,12] its energy efficiency of roughly 90% greatly surpasses the 2 – 5% achieved by laser-based AM.[13,14] Thanks to their favorable welding characteristics, aluminum–copper (Al–Cu) alloys serve as ideal materials for WAAM fabrication.[15-17] The bead geometry, which represents the basic fabrication unit in WAAM, exerts a direct influence on the dimensional fidelity of the manufactured component. Inadequate bead quality requires additional finishing operations, thereby increasing labor expenditure and leading to material wastage.

Recently, the laser-arc hybrid approach to additive manufacturing has come to the forefront of scholarly interest. By steering the arc, the laser decreases its electrical resistance and field strength, which in turn improves arc stability and boosts the build rate.[18] When the two energy sources are coupled, inverse bremsstrahlung further augments laser-energy uptake, and the laser improves melt-pool convection as well as the homogeneity of elemental distribution.[19] Even so, integrating laser and arc complicates the multiphysics interactions, greatly raising the challenge of forecasting weld-bead dimensions. Consequently, the precise prediction of weld-bead geometry in laser-arc hybrid additive manufacturing (LAHAM) emerges as a pivotal problem that demands prompt resolution.

As an essential subdivision of artificial intelligence (AI), machine learning (ML) identifies patterns through data analysis and leverages them for prediction and decision-making tasks.[20] During the past decade, ML has found broad applications across numerous domains, such as medical diagnostics,[21] forecasting material properties,[22] intelligent manufacturing,[23] self-driving vehicles,[24] natural language processing,[25] and object detection.[26] A synopsis of research forecasting the links between process parameters and layer geometry in MAM is provided in Table 1. Using laser power and scan speed as predictors, Le-Hong *et al.*[27] developed random-forest and artificial-neural-network models to estimate layer geometry in laser PBF, reporting validation R^2 values exceeding 90%. With laser power, travel speed, and powder feed rate as variables, Zhu *et al.*[28] employed support vector regression (SVR) to predict the layer height and width of DED, reaching 93% accuracy. Deploying a naïve Bayes approach, Liu and Kuo[29] studied wire-laser DED; by inputting travel velocity, laser power, and wire feed speed, they predicted bead dimensions, yielding R^2 values of 91% and 94%. Xia *et al.*[30] employed a genetic-algorithm-tuned adaptive neuro-fuzzy inference system model to estimate surface roughness from wire feed and welding speeds, achieving validation R^2 values exceeding 90%. Oh *et al.*[31] introduced an SVR model into the WAAM process, using key parameters such as welding current and wire feed rate to accurately predict bead width and height and to identify geometric non-uniformity defects that may arise under different operating conditions. Šket *et al.*[32] used an extreme gradient boosting (XGBoost) regression model, with current and travel speed as the two process parameters, to predict the geometric morphology of the weld bead.

Table 1. Overview of research on data modeling between process parameters and layer geometries in metal additive manufacturing

Process	Models	Inputs	Outputs	Ref.
LPBF	RF and ANN	Laser power and scanning velocity	Layer height, width, and penetration depth	27
Powder-laser DED	SVR	Laser power, travel speed, and powder feed rate	Layer height and width	28
Wire-laser DED	NB	Laser power, travel speed, and wire feed rate	Layer height and width	29
WAAM	ANFIS	Wire feed rate and travel speed	Surface roughness	30
WAAM	SVR	Wire feed rate and travel speed	Layer height and width	31
WAAM	XGBoost	Current and travel speed	Layer height, width, and area	32

Abbreviations: ANFIS: Adaptive neuro-fuzzy inference system; ANN: Artificial neural network; DED: Directed energy deposition; LPBF: Laser powder bed fusion; NB: Naïve Bayes; RF: Random forest; SVR: Support vector regression; WAAM: Wire arc additive manufacturing; XGBoost: Extreme gradient boosting.

Despite these advances in predicting layer geometries of MAM based on process parameters, reliable estimation of bead size in LAHAM still confronts significant challenges. The link between LAHAM processing parameters and

bead dimensions is both intricate and non-linear, calling for further intensive study. Because individual regression models are constrained by their respective hypothesis spaces, no single model can guarantee an optimal result; therefore, ensemble schemes that combine multiple models[33] are generally employed to enhance prediction accuracy. Put differently, simple ML or neural-network approaches alone may not suffice, whereas more elaborate ensemble architectures are able to offer superior predictive accuracy. In addition, incorporating explainable-analysis methods enables researchers to grasp data features more thoroughly and to probe the effect of process parameters on bead-geometry predictions. These analytic approaches, once validated, support investigators in deepening their data understanding and hence in assessing more precisely the impact of process parameters on predictive outcomes.

Herein, we present a particle swarm optimization (PSO)-based ensemble predication (PSO-EP) that combines four base models – Gaussian process regression (GPR), SVR, artificial neural networks (ANN), and extreme learning machines (ELM) – with PSO employed to calibrate their respective weights. The predictive capability of PSO-EP is benchmarked against single base learners and alternative ensemble methods, and the results verify the superiority of the proposed approach. In addition, based on Shapley theory, an interpretability study is carried out in which visual tools, including feature-importance and sample-distribution charts, afford deeper insights into how individual features and samples sway the predictive results.

2. Materials and methods

2.1. Experimental setup

The system utilized in this study is depicted in Figure 1. In the system, the composite heat source is composed of a welding machine (Fronius CMT Advanced 4000R, Austria) and a fiber laser system (Raycus RFL-C3300W, China). The fiber laser system consists of a laser source, an output head, and a cooling unit, with the relative position of the laser output head and the welding gun is illustrated in Figure 1. Line structured light (Gocator 2430, Canada) was utilized to obtain the point cloud data of the weld bead morphology. The procedure of laser-scanning the actual weld bead morphology and generating the point cloud is depicted in Figure 2. The motion platform used is a CNC machine tool (Fana FA2818HG, China). The deposition material is ER2319 aluminum alloy (1.2 mm diameter), and the base material is 2219 aluminum alloy. During the manufacturing process, the welding mode was cold metal transfer pulse advance (CMT-PADV), with the laser CMT process parameters listed in Table 2. Before the experiment, the substrate was processed and cleaned with acetone. The chemical compositions of the substrate and the wire are provided in Table 3.

2.2. Experiment design

Within the WAAM process, the weld bead dimensions are strongly affected by the choice of process parameters. An increase in wire feed speed leads to greater weld bead width and height.[34] A larger arc length adjustment broadens the bead width, whereas a higher pulse correction decreases its height.[35] Within LAHAM, an optimal laser power level supports geometric uniformity, whereas overly high power causes size variability.[36] Accordingly, this study concentrates on the influence of wire feed speed (v_w), welding speed (v_t), arc length correction (l), pulse correction (f), and laser power (p) on weld bead width (W) and height (H).

In Figure 3, the full factorial design with three factors at three levels and the Box–Behnken design are depicted schematically. The Box–Behnken design,[37] as opposed to the full factorial design, prevents extreme condition combinations and efficiently captures second-order effects with a reduced number of experiments, and was therefore employed in this work. First, this study followed the process window recommended in reference[38] and employed single-factor screening experiments to define the valid ranges of each influencing factor, encoding their upper and lower bounds as +1 and −1, respectively; the selected key factors and their symbols are detailed in Table 4. Table 5 displays the 46 coded experimental conditions and outcomes. Table 6 comprises 20 randomly sampled process parameter configurations and associated weld geometry metrics, used as the validation and test datasets. To assess the reproducibility of the experimental dataset, six repeated trials were conducted under the central-point parameter configuration, and the coefficient of variation (CV)[39] was employed for evaluation. The analysis revealed CV values of 3.25% for bead width and 2.74% for bead height – both markedly lower than the commonly accepted 10% benchmark[40] – providing strong evidence of high data consistency. As illustrated in Figure 4, all the weld beads were well-formed and defect-free. The overall experimental count was determined based on Equation I.

$$N = 2q(q-1)+C_0 \quad \text{(I)}$$

where q is the number of experimental parameters, and C_0 denotes the number of repetitions needed to minimize errors arising from environmental and human factors. In this paper, q is 5, and C_0 is 6.

2.3. Particle swarm optimization-based ensemble prediction

In the proposed ensemble forecasting framework, the four base learners – ANN, GPR, SVR, and ELM – are first

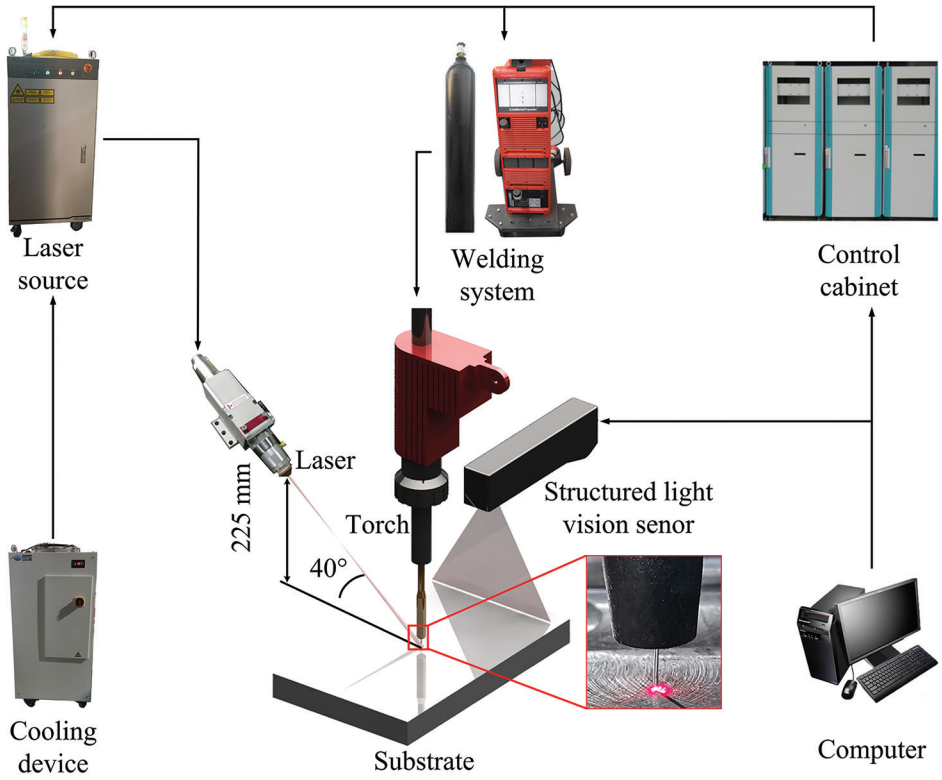

Figure 1. Schematic illustration of the laser-arc hybrid additive manufacturing system

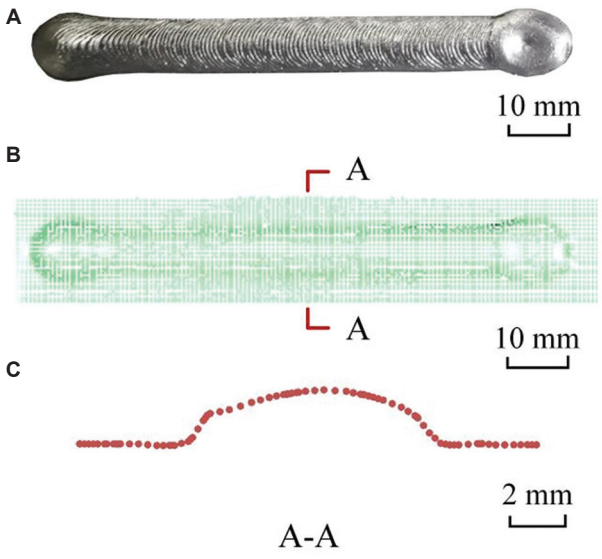

Figure 2. Schematic diagram shows the quantification of weld-bead width and height. (A) Actual morphology of a weld bead in the training set. (B) 3D point cloud obtained through line-laser scanning. (C) Extracted weld-bead contour

subjected to hyperparameter optimization and training on the training and validation datasets. The tuned models are subsequently deployed on the test set, where they each yield their own prediction outputs. Thereafter, particle swarm optimization (PSO) iteratively updates the weights of the models, driving the weighted prediction error downward until convergence and ultimately producing an ensemble prediction that fuses the four models. Finally, in accordance with Equation II, the mean absolute percentage error is calculated for each base model as well as for the ensemble.

$$MAPE = \frac{1}{n}\sum_{i=1}^{n}\frac{\left|y_i - \widehat{y_i}\right|}{y_i} \times 100\% \quad \text{(II)}$$

Particle swarm optimization is a global optimization technique inspired by swarm intelligence, which locates optima by modeling the coordinated, iterative movement of many particles within a multidimensional search domain. Every particle acts as a potential solution; its velocity and position are continually updated with reference to its personal best and the swarm's global best, which hastens convergence and elevates search efficiency.

To simplify the weight optimization for multi-model ensembles, we introduce, under the PSO paradigm, a one-dimensional discrete index encoding (ODIE) that assigns weights to the base regression models with high efficiency.

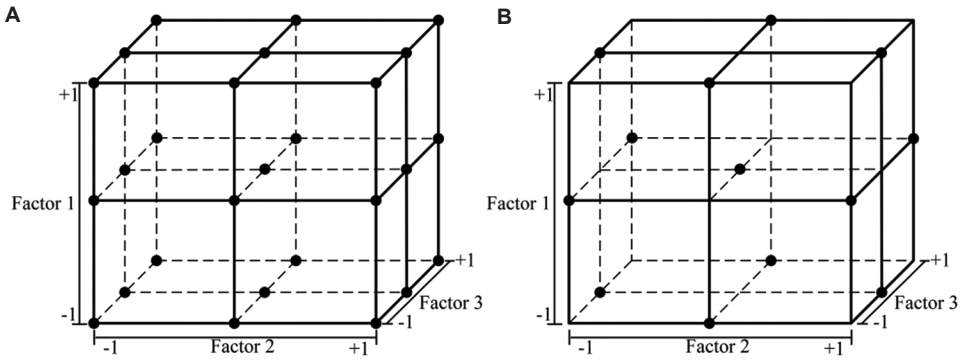

Figure 3. Sketch of three-factor three-level experimental designs. (A) Full factorial design. (B) Box–Behnken design

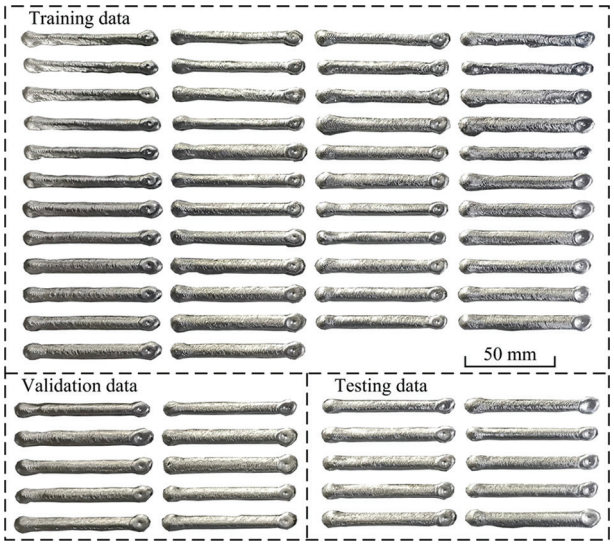

Figure 4. The actual morphology of the 46 weld beads in the training dataset

In traditional methods (Figure 5A), weights are usually expressed as a D-dimensional continuous vector:

$$X = [x_1, x_2, ...x_D], \sum_{i=1}^{D} x_i = 1 \quad \text{(III)}$$

Traditional methods usually encode the weight vector as a D-dimensional continuous variable and perform iterative updates of particle velocities and positions in this high-dimensional space. Nevertheless, this design entails two principal drawbacks: On the one hand, owing to the excessive dimensionality of the search space, PSO tends to converge slowly when optimizing in a D-dimensional continuous domain. On the other hand, to enforce the normalization constraint $\sum_{i=1}^{D} x_i = 1$, the weights must be projected back or a penalty term introduced after every iteration, thereby complicating implementation and further burdening hyperparameter tuning.

Table 2. Process parameters of the laser-CMT process

Heat source	Parameter	Value
CMT	Wire feeding speed (m/min)	6
	Travel speed (mm/min)	600
Laser	Laser power (kW)	3
	Defocusing length (mm)	171.5

Abbreviation: CMT: Cold metal transfer.

Table 3. Wire and substrate chemical compositions

Alloy	Chemical components (wt.%)								
	Si	Fe	Cu	Mn	Mg	Zn	V	Ti	Zr
ER2319 (wire)	0.106	0.156	5.950	0.273	0.009	0.012	0.068	0.104	0.104
2219-T6 (substrate)	0.021	0.100	6.060	0.270	<0.01	0.024	0.092	0.039	0.130

Abbreviations: Si: Silicon; Fe: Iron; Cu: Copper; Mn: Manganese; Mg: Magnesium; Zn: Zinc; V: Vanadium; Ti: Titanium; Zr: Zirconium.

Table 4. Process control parameters and their levels

Parameters	Units	Notation	Factor levels		
			−1	0	1
Wire feed speed	m/min	v_w	6	7	8
Welding speed	mm/min	v_t	500	600	700
Arc length correction	%	l	5	10	15
Pulse correction	%	f	0	1	2
Laser power	kW	p	1	2	3

In the ODIE workflow (Figure 5B), every particle is encoded as an integer sequence of length k:

$$X = [x_1, x_2, .., x_k], x_i \in \{0, 1., D-1\} \quad \text{(IV)}$$

In this setting, D represents the total count of base learners, and x_i indicates the index of the base model chosen at position i. The weight of each base model j can be

Table 5. Design matrix and targets

Experimental run	Design matrix					Results	
	v_w	v_t	l	f	p	W (mm)	H (mm)
1	7	600	5	2	2	8.19	2.78
2	7	600	10	1	2	8.49	2.69
3	8	600	10	1	1	7.66	3.14
4	8	700	10	1	2	7.14	2.54
5	7	600	10	1	2	7.85	2.60
6	7	600	15	0	2	6.70	2.77
7	7	700	5	1	2	7.28	2.56
8	7	500	5	1	2	9.13	2.76
9	6	600	5	1	2	7.52	1.89
10	8	600	5	1	2	8.44	2.92
11	7	600	5	1	3	8.62	2.45
12	7	700	10	1	3	7.09	2.11
13	7	600	10	2	3	9.63	2.12
14	6	600	10	1	3	7.30	2.32
15	6	600	15	1	2	6.86	2.76
16	8	600	10	1	3	9.70	2.35
17	7	600	10	1	2	8.36	2.52
18	7	700	10	1	1	7.53	2.55
19	7	500	10	1	3	10.1	2.56
20	7	600	5	1	1	9.01	2.42
21	6	700	10	1	2	7.25	2.54
22	7	600	15	2	2	8.75	2.72
23	6	500	10	1	2	7.79	2.56
24	7	500	10	2	2	9.44	2.86
25	7	700	10	2	2	7.83	2.38
26	8	600	15	1	2	8.78	2.52
27	7	600	10	2	1	8.14	2.92
28	6	600	10	2	2	7.84	2.48
29	8	600	10	2	2	8.65	2.68
30	7	700	10	0	2	7.02	2.44
31	7	700	15	1	2	7.73	2.40
32	6	600	10	1	1	7.78	2.36
33	7	600	15	1	3	9.20	2.04
34	7	600	10	0	3	8.47	2.24
35	7	600	5	0	2	8.95	2.44
36	7	600	10	1	2	8.49	2.61
37	7	600	15	1	1	7.77	2.93
38	7	500	10	0	2	8.47	2.71
39	8	600	10	0	2	8.98	2.64
40	7	500	10	1	1	8.36	3.00
41	7	600	10	1	2	8.61	2.49
42	7	600	10	0	1	8.15	2.56
43	8	500	10	1	2	10.17	3.02
44	6	600	10	0	2	7.01	2.40
45	7	600	10	1	2	8.49	2.59
46	7	500	15	1	2	9.07	3.12

(Cont'd...)

Table 5. ***(Continued)***

Abbreviations: f: Pulse correction; H: Weld bead height; l: Arc length correction; p: Laser power; v_t: Welding speed; v_w: Wire feed speed; W: Weld bead width.

Table 6. Experimental data for the validation and test sets

Experimental run	Design matrix					Results	
	v_w	v_t	l	f	p	W (mm)	H (mm)
1	6.50	510.00	6.00	1.50	1.20	8.69	2.56
2	6.30	540.00	8.00	1.70	2.70	8.91	2.45
3	6.60	570.00	7.00	0.20	2.20	8.30	2.47
4	7.90	530.00	7.00	0.90	1.80	9.36	3.01
5	7.20	520.00	6.00	0.30	2.90	9.64	2.52
6	7.80	510.00	12.00	0.50	1.50	8.55	3.13
7	7.30	620.00	12.00	1.20	1.60	8.19	2.69
8	6.30	580.00	14.00	1.10	1.00	7.31	2.95
9	7.00	680.00	14.00	1.30	2.00	7.57	2.41
10	8.00	540.00	14.00	1.10	2.80	10.50	2.46
11	6.30	610.00	6.00	0.50	2.30	7.89	2.25
12	6.30	660.00	6.00	0.60	1.50	7.87	2.20
13	6.60	570.00	10.00	0.20	2.00	7.78	2.51
14	6.80	550.00	14.00	1.60	1.20	8.31	3.07
15	7.30	520.00	11.00	1.80	1.30	8.68	3.12
16	6.70	550.00	13.00	0.30	1.20	7.26	2.92
17	7.90	690.00	10.00	0.80	1.20	7.33	2.71
18	7.30	620.00	7.00	1.90	1.00	7.92	2.64
19	6.90	640.00	9.00	1.60	2.70	8.56	2.28
20	7.10	520.00	7.00	1.30	1.80	9.04	2.86

Abbreviations: f: Pulse correction; H: Weld bead height; l: Arc length correction; p: Laser power; v_t: Welding speed; v_w: Wire feed speed; W: Weld bead width.

obtained by tallying its occurrences n_j within the sequence, thus allowing direct decoding:

$$\omega_j = \frac{n_j}{k}, \sum_{j=1}^{D} \omega_j = 1 \quad \text{(V)}$$

The encoding intrinsically meets the normalization requirement without extra projection or penalty terms,

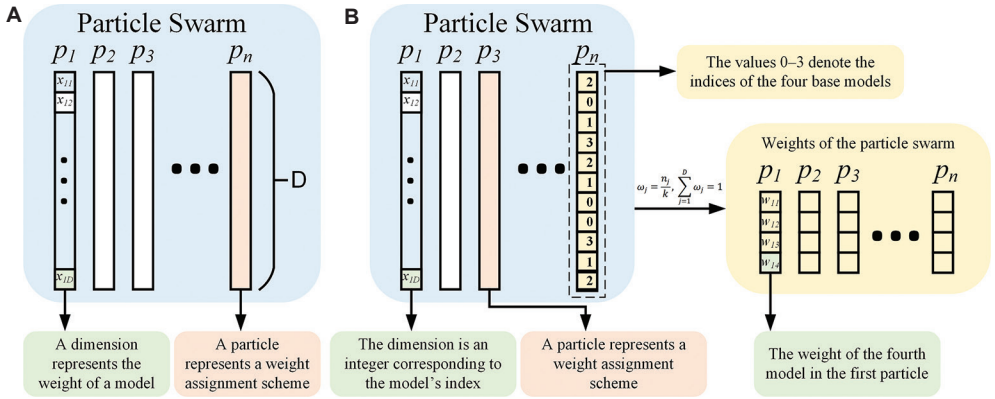

Figure 5. Comparison between traditional particle swarm optimization (PSO) encoding and one-dimensional discrete index encoding: (A) Traditional encoding, and (B) one-dimensional discrete index encoding

and by collapsing the search space from a D-dimensional continuum to a single discrete index, it significantly cuts computational complexity and speeds up convergence.

Figure 6 presents the operational flow of the PSO-driven ensemble learning module. Initially, a swarm of particles is randomly seeded within the one-dimensional discrete index space, where every particle encodes a particular distribution of weights across the base learners. Subsequently, each particle is decoded, the weight of each base model is determined from the index frequencies, and an ensemble prediction is produced accordingly. The error between the predicted and true values is then used as the fitness, driving the velocity and position updates of PSO. During iteration, each particle adjusts its position through a weighted combination of inertia, cognitive, and social components, balancing global exploration and local exploitation. Meanwhile, the historically best particle is retained, and random perturbations are introduced to preserve swarm diversity. Once the termination criterion is met, the global best particle is decoded to yield the optimal weight allocation for the base models.

The specific workflows of the base learners and the PSO iterative optimization are described in detail in the literature.[41-44] Every baseline model was built in a Python environment with the scikit-learn library, and the PSO routine was carried out using the PySwarms toolkit.

2.4. Shapley-based explainable analysis

Despite the widespread use of ML models in pivotal domains such as biomedicine and self-driving technology, their decision paths remain largely inscrutable black boxes, eroding user confidence and hindering real-world implementation. To tackle this challenge, explainable ML has risen to prominence, seeking to illuminate model workings, pinpoint key predictors, and use that knowledge to drive performance improvements. The present work

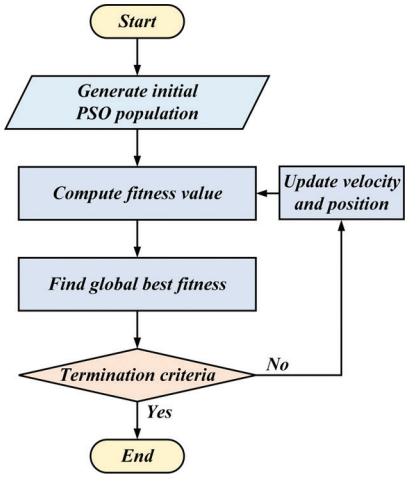

Figure 6. Flow chart of particle swarm optimization-based ensemble module

performed an explainability analysis of the process parameters, isolating the factors that strongly influence bead size and furnishing direction for future model refinement. Proposed by Shapley in 1952,[45] the Shapley value offers a fair way to allocate rewards in cooperative games by measuring every player's marginal contribution. SHapley Additive exPlanations (SHAP), a Python library for *post hoc* model explanation, evaluates the influence of a feature on the output by calculating its marginal contributions over all subset combinations, yielding global importance orders as well as case-specific interpretations. Given the full feature set F, the SHAP value for feature *j* is defined by:

$$\varphi_j^{(i)} = \sum_{S\subseteq\{m_1,\ldots m_o\}\setminus\{m_j\}} \frac{|S|!(o-|S|-1)!}{o!}\left(val(S\cup\{m_j\}) - val(S)\right) \quad \text{(VI)}$$

SHAP represents a paradigmatic *post hoc* interpretability technique, revealing feature–output relationships through

visualization. The study began by calculating SHAP values for every feature, thereby quantifying their influence on the predictions; the original features were then contrasted with newly derived ones to confirm the performance gains attributable to the new attributes. Subsequently, the SHAP visualization toolkit was employed to depict feature importance and the directionality of their effects, affording a deeper dissection of the model's reasoning process.

2.5. Parameter setting of the PSO-EP

The training set trained multiple regression models, while five-fold cross-validation on the validation set tuned their hyperparameters. Once tuning was completed, the model with the best validation performance was chosen to forecast bead size on the test set; these forecasts constituted the response values. Next, the response values together with the models' evaluation indices were fed into the ensemble module, which used the metric of Equation II as a fitness function and applied PSO to derive a weighted fusion of the individual outputs. Within the PSO-EP method, the weight-assignment stage employed up to 50,000 iterations and a swarm of 200 particles. Iterative search ultimately yielded the optimal set of model weights, and a consolidated estimate of bead dimensions was output. The PSO-EP approach was further benchmarked against various alternative techniques to evaluate its efficacy.

2.6. Model evaluation indicators

Once the prediction was complete, the model's performance was assessed by computing the error between the true values and the predicted results for the test data. Smaller errors indicated better model performance. For the regression problem concerning the LAHAM weld bead width and height, this study used mean absolute error (MAE), root mean squared error (RMSE), and coefficient of determination (R^2) as performance metrics. MAE and RMSE assess the deviation between predicted and actual values, with RMSE being more sensitive to larger errors. R^2 reflects the model's ability to explain the variability in the data, with values closer to 1 indicating a better fit. A comprehensive evaluation of model performance can be achieved by integrating these metrics.

$$MAE = \frac{1}{n}\sum_{i=1}^{n} | y_i - \widehat{y_i} | \quad \text{(VII)}$$

$$RMSE = \sqrt{\frac{1}{n}\sum_{i=1}^{n}(y_i - \hat{y}_i)^2} \quad \text{(VIII)}$$

$$R^2 = 1 - \frac{\sum_i \left(\hat{y}_i - y_i\right)^2}{\sum_i \left(y_i - \overline{y}\right)^2} \quad \text{(IX)}$$

3. Results and discussion

In this study, the validity of the proposed PSO-EP method was demonstrated. For performance evaluation, the PSO-EP's predictions were initially benchmarked against each single base model to measure gains in prediction precision. Subsequently, it was assessed alongside other widely used ensemble forecasting approaches to underscore the PSO-EP's overall superiority. Finally, an importance analysis of the process parameters was conducted to uncover their individual impacts on the prediction outcomes.

3.1. Comparison of PSO-EP with base models

To assess the superiority of PSO-EP, the present study conducted a comparison against four baseline models: GPR, SVR, ANN, and ELM. Figures 7 and 8 illustrate the performance of the models in the prediction tasks for weld bead width and height, respectively. To facilitate a clear comparison, the figures display only the test set predictions along with their respective error curves.

Figure 7 illustrates that PSO-EP excels in weld bead width prediction, with an R^2 of 0.9567, markedly outperforming GPR, SVR, ANN, and ELM, which signifies its enhanced capability to accurately capture the overall width variation trend; simultaneously, PSO-EP records the smallest RMSE and MAE values, substantiating its lowest overall prediction error and MAE (Table 7). Nevertheless, the highest relative error observed in extreme samples is 5.6%, which is only superior to ANN's 7.8%, indicating potential for further enhancement in limiting the maximum error. Sample 6 showed a comparatively large error in weld bead width prediction. The feature importance analysis in section 3.3 indicated that wire feed speed and welding speed are the key factors determining width; for this sample, the wire feed speed was 7.80 m/min and the welding speed was 510 mm/min. Figure 9 reveals that this set of parameters is positioned at the boundary of the process window, where their interaction drives an increase in bead width, resulting in an overestimation by the model and a magnified error. This finding suggests, first, that the model's generalization at the boundary of the parameter space can be further enhanced; second, that because this condition approaches the experimental limit, sporadic experimental inaccuracies could also exacerbate the prediction error.

Regarding weld bead height prediction (Figure 8), while all models display comparable overall trend curves, PSO-EP notably excels in fitting regions with pronounced height fluctuations, where its predicted curve almost perfectly overlaps with observed values; by comparison, GPR, SVR, ANN, and ELM show evident discrepancies at

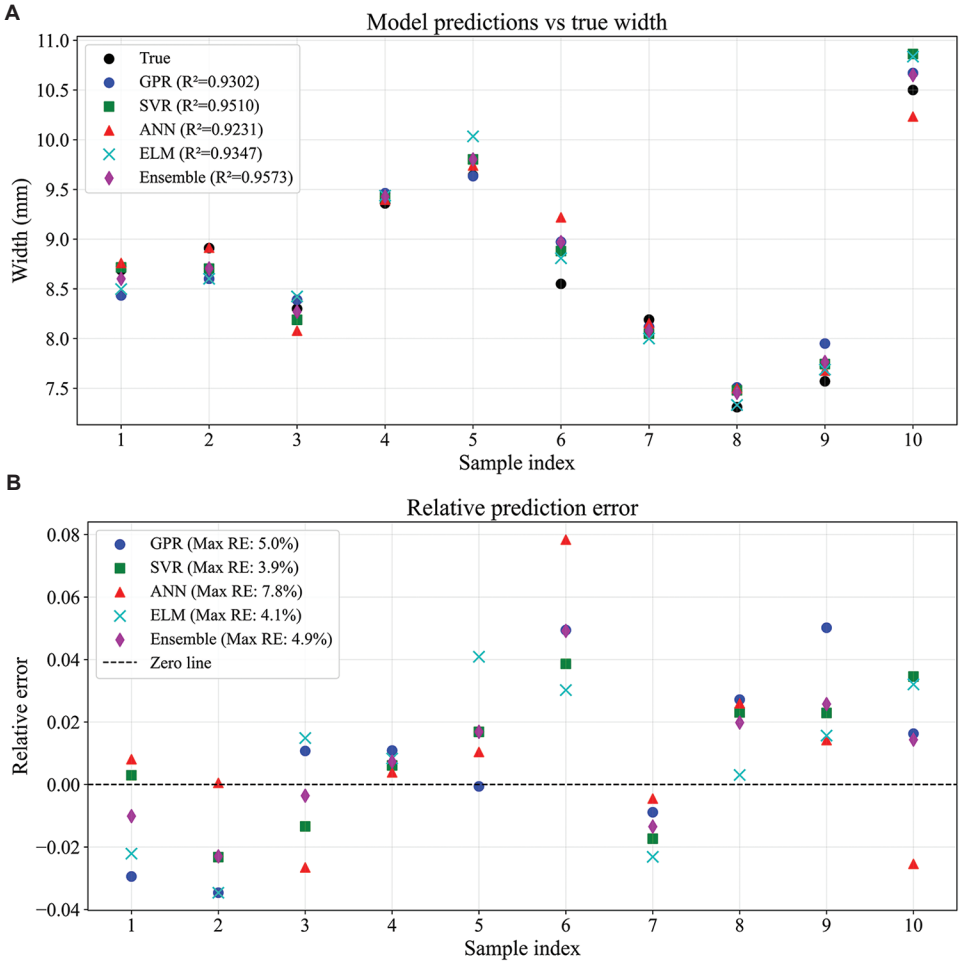

Figure 7. Predicted values (A) and error performance (B) of each model in the width prediction task
Abbreviations: ANN: Artificial neural network; ELM: Extreme learning machines; GPR: Gaussian process regression; SVR: Support vector regression

Table 7. Evaluation metrics of each model in the width prediction task

Model	MAE	RMSE	R^2
GPR	0.2006	0.2400	0.9302
SVR	0.1741	0.2012	0.9510
ANN	0.1704	0.2519	0.9231
ELM	0.2021	0.2322	0.9347
PSO-EP	0.1454	0.1890	0.9567

Abbreviations: ANN: Artificial neural network; ELM: Extreme learning machines; GPR: Gaussian process regression; MAE: Mean absolute error; PSO-EP: Particle swarm optimization-based ensemble prediction model; R^2: Coefficient of determination; RMSE: Root mean squared error; SVR: Support vector regression.

fluctuation points, struggling to precisely represent height changes. Quantitative assessment showed that the PSO-EP achieved an R^2 of 0.9492 (Table 8), again leading all models, with RMSE and MAE metrics below those of competitors; its maximum relative error stood at 4.2%, ranking second to SVR, confirming PSO-EP's outstanding precision and robustness in the weld bead height prediction task.

3.2. Comparison of PSO-EP with other ensemble methods

Figure 10 presents a comparison of four ensemble forecasting approaches: the averaging method,[46] Stacking,[47] ELGA,[48] and the PSO-EP method introduced herein. Results indicated that PSO-EP attained an R^2 of 0.9492 in predicting weld bead height, surpassing the averaging method (0.9387) by 1.12%, stacking (0.9378) by 1.22%, and ELGA (0.9206) by 3.11%. For weld bead width prediction, PSO-EP achieved an R^2 of 0.9567, which is 2.07% higher than the averaging method (0.9373), 3.47% higher than stacking (0.9246), and 2.36% higher than ELGA (0.9346). These notable improvements stem from the PSO algorithm's effective global optimization ability.

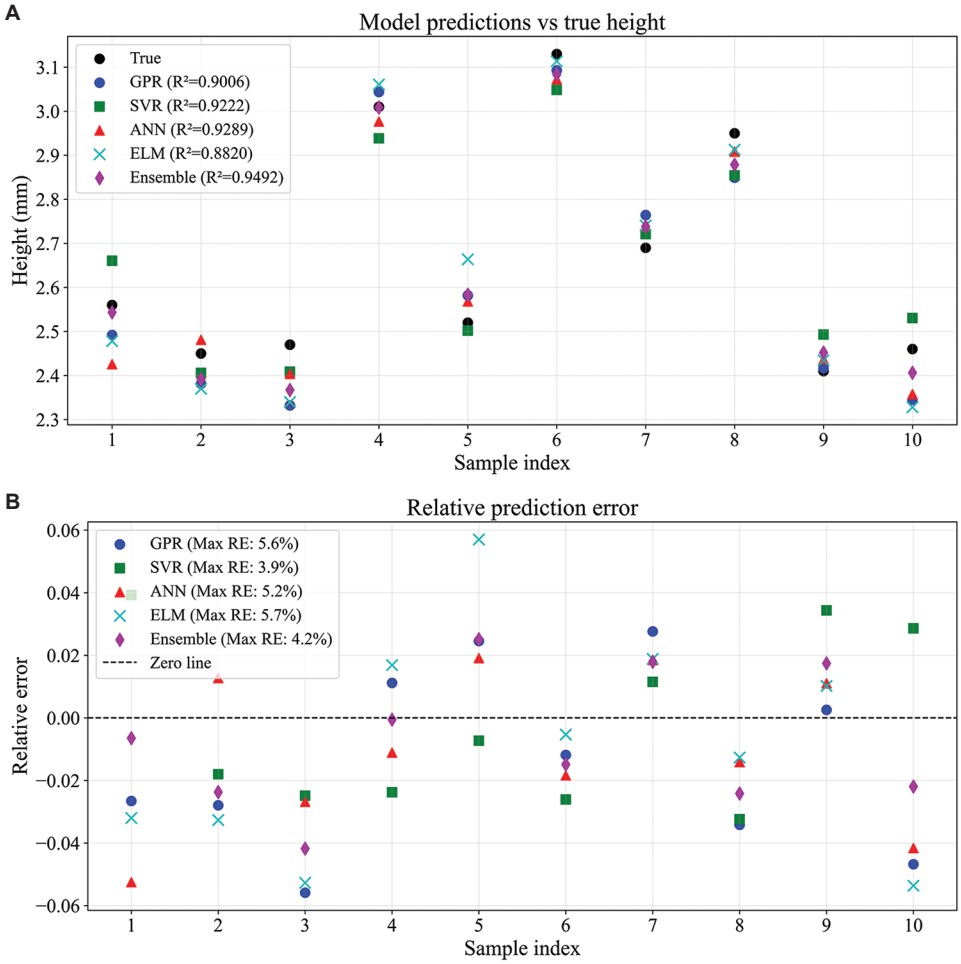

Figure 8. Predicted values (A) and error performance (B) of each model in the width prediction task
Abbreviations: ANN: Artificial neural network; ELM: Extreme learning machines; GPR: Gaussian process regression; SVR: Support vector regression

Table 8. Evaluation metrics of each model in the height prediction task

Model	MAE	RMSE	R^2
GPR	0.0704	0.0798	0.9006
SVR	0.0657	0.0706	0.9222
ANN	0.0591	0.0675	0.9289
ELM	0.0748	0.0869	0.8820
PSO-EP	0.0505	0.0571	0.9492

Abbreviations: ANN: Artificial neural network; ELM: Extreme learning machines; GPR: Gaussian process regression; MAE: Mean absolute error; PSO-EP: Particle swarm optimization-based ensemble prediction model; R^2: Coefficient of determination; RMSE: Root mean squared error; SVR: Support vector regression.

3.3. SHAP analysis

In this section, the association between processing parameters and prediction results is examined through Shapley theory. This theory computes the marginal contribution of each feature within various feature subsets, then derives a weighted average to quantify each feature's impact on the prediction, termed the SHAP value. Figures 11 and 12 illustrate the ranked importance of process parameters within the width and height models, facilitating insight into each parameter's effect on the model. In the figures, each row corresponds to a parameter, the x-axis displays SHAP values, the dot color reflects the feature magnitude, and the order is determined by the average absolute SHAP value over all samples. For predicting weld bead width, welding speed is paramount and inversely correlated with width because increased speed hastens melt pool cooling, reduces metal fill time, and narrows the bead. Wire feeding rate and laser power exhibit positive correlations with width, facilitating bead growth by augmenting metal deposition and raising melt pool temperature, respectively. Arc length and pulse corrections exert limited influence, fine-tuning heat input to modulate width changes. For weld bead height prediction,

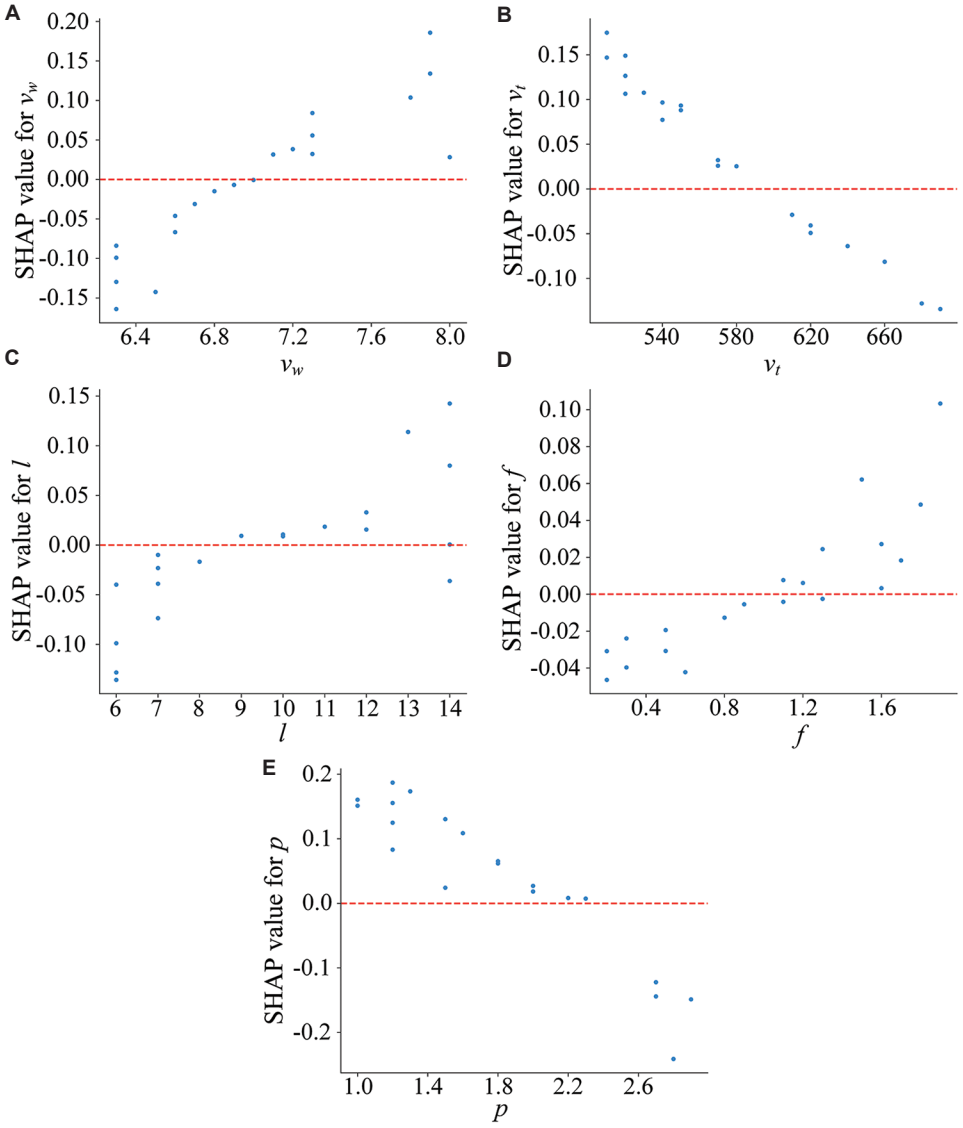

Figure 9. Process parameter dependence plots in the height prediction task: (A) Wire feed speed (v_w), (B) Welding speed (v_t), (C) Arc length correction (l), (D) Pulse correction (f), and (E) Laser power (p)

laser power is the dominant parameter and inversely related to height, since increased lateral expansion restricts vertical accumulation. Welding speed similarly exhibits a negative correlation because increased speed promotes faster cooling, thereby limiting height increase. The wire feed rate shows a positive correlation by promoting vertical deposition. Despite their limited impact, arc length and pulse corrections are positively associated with height, contributing to height enhancement.

Dependence plots serve as crucial instruments to examine how feature values impact prediction results. Figure 13 depicts the relationships between process parameters and weld bead width. With increasing wire feed rate, SHAP values increase markedly, demonstrating positive promotion; below 6.9 m/min, the effect is negative, shifting to positive above this point, resulting in bead width expansion. SHAP values for welding speed are positive under 580 mm/min, fostering width increase, but become negative beyond this threshold, limiting bead expansion. For laser power under 2.3 kW, SHAP values are negative, signifying width limitation at low power; beyond this, the influence turns positive, markedly enhancing bead width. Figure 9 further presents the relationships between process parameters and weld bead height. The influence patterns of wire feed speed, welding speed, and laser power on weld bead height prediction resemble those

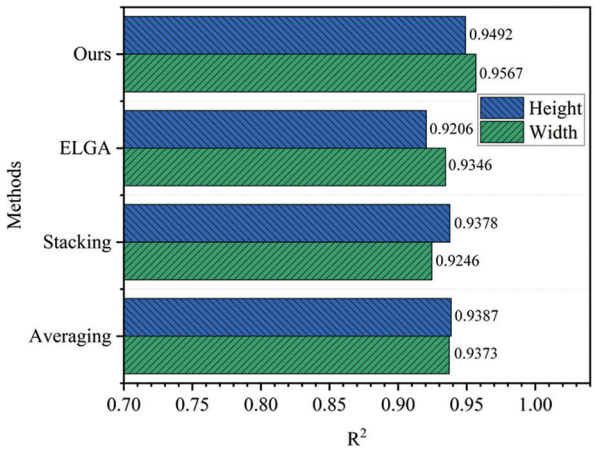

Figure 10. Comparative analysis of various ensemble forecasting approaches

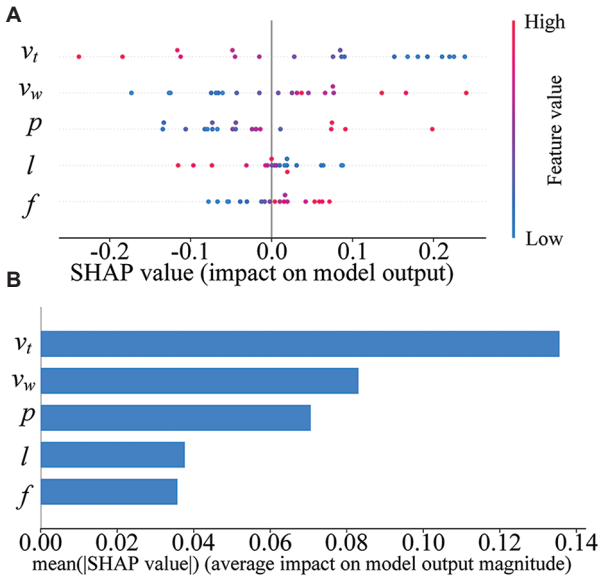

Figure 11. Importance ranking of process parameters in the width prediction task. (A) SHAP summary plot. (B) Importance plot of process parameter
Abbreviations: f: Pulse correction; *l*: Arc length correction; *p*: Laser power; v_t: Welding speed; v_w: Wire feed speed, SHAP: SHapley Additive exPlanations

observed for bead width. Below 7 m/min, wire feed speed has a negative influence, which reverses to positive when exceeding this value, facilitating height growth. Welding speed exhibits a positive correlation under 580 mm/min, shifting to a negative correlation beyond 610 mm/min, thereby inhibiting height increase. Below 2.3 kW, laser power positively correlates with height, but the relationship reverses above this threshold, restricting height growth. In summary, clear thresholds exist for process parameters affecting weld bead width and height, beyond which

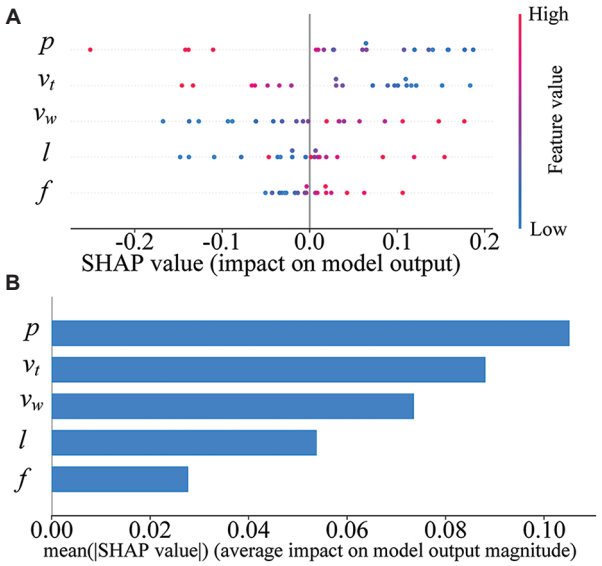

Figure 12. Importance ranking of process parameters in the height prediction task. (A) SHAP summary plot. (B) Importance plot of process parameter
Abbreviations: f: Pulse correction; *l*: Arc length correction; *p*: Laser power; v_t: Welding speed; v_w: Wire feed speed, SHAP: SHapley Additive exPlanations

their effects may invert, thereby affecting the quality of formation.

3.4. Conceptual framework for bead size and shape prediction applied to in-process characterization

Figure 14 depicts the initial stage of the additive manufacturing process, in which the 3D model is first sliced and a deposition path is generated; the slicing operation defines the layer thickness, and the path planning sets the track width and selects the appropriate process settings accordingly. This study concentrates on the high-precision prediction of bead geometry.

Despite the high accuracy achieved in predicting bead morphology, variations in material batches and environmental fluctuations may still prevent the optimized process parameters from faithfully reproducing the target dimensions. Additional dimensional deviations can arise from tool wear, calibration errors, drifts in laser or arc power, and fluctuations in wire-feed rate. To address these issues, we propose embedding the high-precision prediction model within an online quality-monitoring and closed-loop control framework to enable real-time correction and stabilization of bead dimensions.

During printing, a melt-pool camera continuously captures images near the welding torch and feeds them to

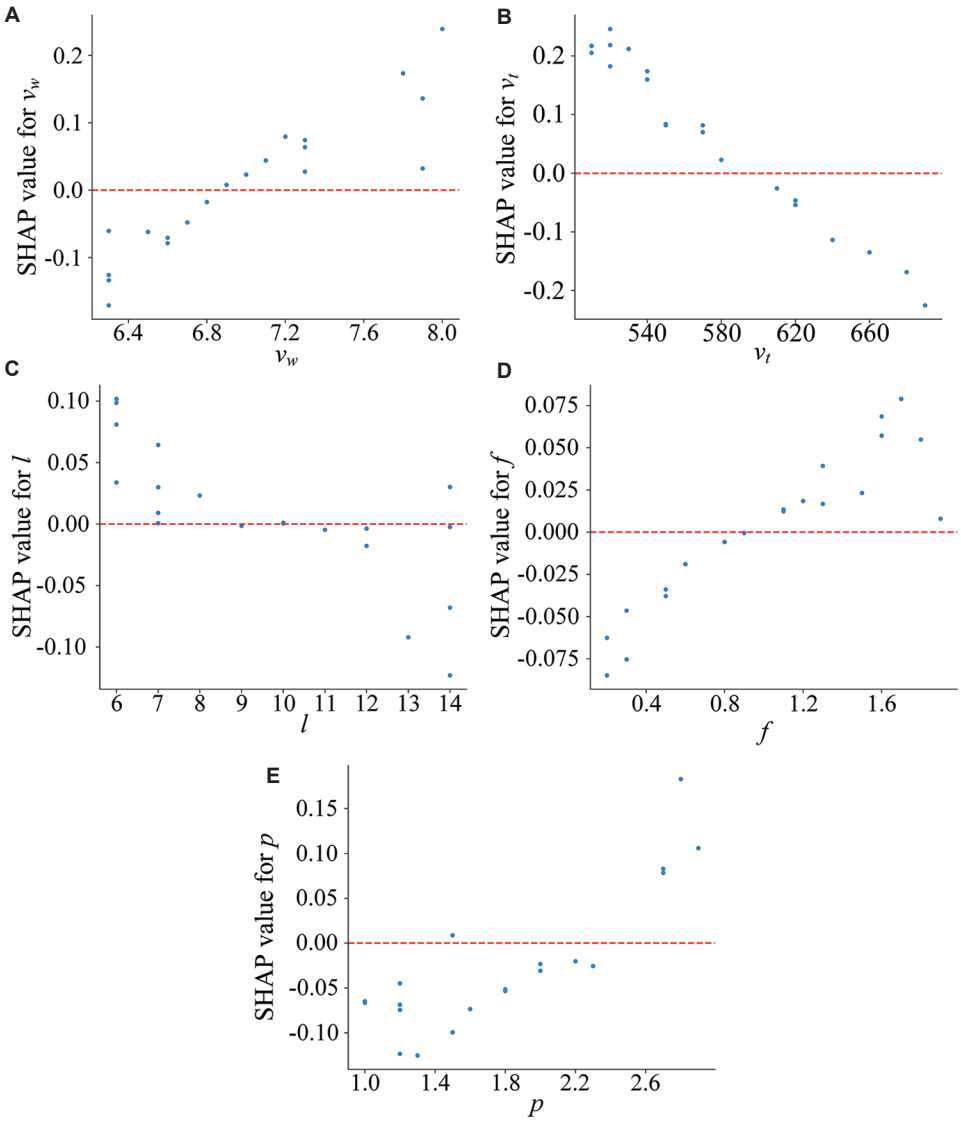

Figure 13. Process parameter dependence plots in the width prediction task: (A) Wire feed speed (v_w), (B) Welding speed (v_t), (C) Arc length correction (l), (D) Pulse correction (f), and (E) Laser power (p)

the trained U-net model, which segments and crops the bead and online extracts the actual bead width W_{real} and height H_{real}. After comparing the measured and desired dimensions, Equations X and XI compute the required correction to obtain new targets W' and H'; these targets feed the accurate bead predictor, which derives revised process parameters and refreshes the G-code. The machine resumes deposition under the updated parameters, the camera repeats image acquisition, and the cycle iterates in a closed loop until the bead size remains inside the specified error band.

$$\Delta W = W - W_{real,} W' = W + \Delta W \quad \text{(X)}$$

$$\Delta H = H - H_{real}, H' = H + \Delta H \quad \text{(XI)}$$

The trajectory of next-generation inspection and monitoring architectures has already been examined in previous works.[49,50] Both studies underscore the considerable potential of AI-driven technologies to deliver more robust defect detection and real-time intervention, thereby substantially enhancing the reliability of additive manufacturing processes. Although these strategies have not yet been implemented in the present study, subsequent work will focus on designing and validating the corresponding control mechanisms with the aim of establishing a fully automated closed-loop quality control system.

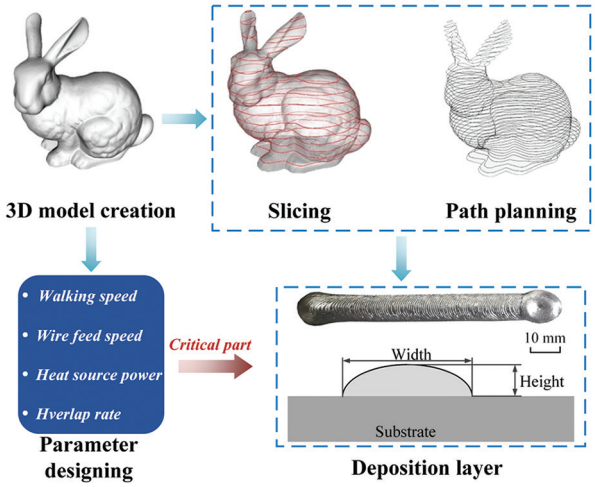

Figure 14. The workflow of path planning

4. Conclusion

In this study, we devised a PSO-driven ensemble regression method, designated PSO-EP, for accurately forecasting weld-bead size in the multiphysics-coupled LAHAM technique. The method leverages PSO to tune the weightings of several base models and, in turn, elevates the aggregate prediction accuracy. The effectiveness of PSO-EP was assessed through extensive comparisons against individual learners (GPR, SVR, ANN, and ELM) and representative ensembles such as averaging, stacking, and ELGA. The findings showed that PSO-EP delivers top-ranked accuracy for predicting both weld-bead width and height.

(1) PSO-EP demonstrated the best performance in weld-bead width prediction, achieving an MAE of 0.1454, an RMSE of 0.1890, and an R^2 of 0.9567; compared with the next-best SVR (R^2 of 0.9510) as well as averaging (R^2 of 0.9373), stacking (R^2 of 0.9246), and ELGA (R^2 of 0.9346), it improved R^2 by 2.07%, 3.47%, and 2.36%, respectively

(2) PSO-EP likewise excelled in predicting weld-bead height, registering an MAE of 0.0505, an RMSE of 0.0571, and an R^2 of 0.9492, substantially surpassing ANN (R^2 of 0.9289), SVR (R^2 of 0.9222), and averaging (R^2 of 0.9387), stacking (R^2 of 0.9378), and ELGA (R^2 of 0.9206), with R^2 gains of 1.12%, 1.22%, and 3.11 %, respectively

(3) SHAP interpretability analysis indicates that weld bead width is primarily influenced by the combined effects of welding speed, wire feed speed, and laser power, whereas weld bead height prediction is driven mainly by laser power and welding speed

(4) Subsequent SHAP threshold analysis uncovered that each process parameter exhibits a threshold above which its influence on weld bead formation can undergo significant shifts in direction or magnitude.

Although the method delivers encouraging results, PSO-EP presently depends on optimizing base model weights within a fixed framework, thereby constraining its flexibility and extensibility. Hence, future studies might explore more self-adaptive or hierarchical ensemble schemes to augment the model's representational capacity and generalization.

Acknowledgments

None.

Funding

This work was financially supported by the CNPC Innovation Foundation (Grant No. 2024DQ02-0306), Innovation and Entrepreneurship Leading Talent Project of Yantai Development Zone in 2022 (Grant No. 2022RC008), Natural Science Foundation of Shandong Province (Grant No. ZR2023QE164), Natural Science Foundation of Qingdao (Grant No. 23-2-1-83-zyyd-jch), and National Natural Science Foundation of China (Grant No. 52405359).

Conflicts of interest

The authors declare no competing interests.

Author's contributions

Conceptualization: Xingwang Bai
Formal analysis: Youheng Fu
Investigation: Boce Xue, Changze Li
Methodology: Kui Zeng
Resource: Yonghui Liu, Yanzhen Zhang
Writing–original draft: Hui Ma, Runsheng Li
Writing–review & editing: Runsheng Li

Ethics approval and consent to participate

Not applicable.

Consent for publication

Not applicable.

Availability of data

Data are available from the corresponding author upon reasonable request.

References

1. Chen X, Fu Y, Kong F, *et al*. An in-process multi-feature data fusion nondestructive testing approach for wire arc additive manufacturing. *Rapid Prototyp J*. 2022;28(3):573-584.

doi: 10.1108/RPJ-02-2021-0034

2. Shi Y, Yan C, Song B, *et al*. Recent advances in additive manufacturing technology: Achievements of the rapid manufacturing center in Huazhong University of science and technology. *Addit Manuf Front*. 2024;3(2):200144.

doi: 10.1016/j.amf.2024.200144

3. Yang Y, Jiang R, Han C, *et al*. Frontiers in laser additive manufacturing technology. *Addit Manuf Front*. 2024;3(4):200160.

doi: 10.1016/j.amf.2024.200160

4. Tan C, Li R, Su J, *et al*. Review on field assisted metal additive manufacturing. *Int J Mach Tools Manuf*. 2023;189:104032.

doi: 10.1016/j.ijmachtools.2023.104032

5. He F, Yuan L, Mu H, *et al*. Research and application of artificial intelligence techniques for wire arc additive manufacturing: A State-of-the-art review. *Robot Comput Integr Manuf*. 2023;82:102525.

doi: 10.1016/j.rcim.2023.102525

6. Qin J, Hu F, Liu Y, *et al*. Research and application of machine learning for additive manufacturing. *Addit Manuf*. 2022;52:102691.

doi: 10.1016/j.addma.2022.102691

7. McNamara K, Ji Y, Lia F, *et al*. Predicting phase transformation kinetics during metal additive manufacturing using non-isothermal Johnson-Mehl-Avrami models: Application to Inconel 718 and Ti-6Al-4V. *Addit Manuf*. 2022;49:102478.

doi: 10.1016/j.addma.2021.102478

8. Kim DO, Lee CM, Kim DH. Determining optimal bead central angle by applying machine learning to wire arc additive manufacturing (WAAM). *Heliyon*. 2024;10(1):e23372.

doi: 10.1016/j.heliyon.2023.e23372

9. Li R, Ju G, Zhao X, *et al*. Simulation of residual stress and distortion evolution in dual-robot collaborative wire-arc additive manufactured Al-Cu alloys. *Virtual Phys Prototyp*. 2024;19(1):e2409390.

doi: 10.1080/17452759.2024.2409390

10. Zhou X, Fang Y, Zhang T, Xiong Z. Retrospective: Advances and opportunities of 3D bioprinting in china over three decades. *Addit Manuf Front*. 2024;3(4):200157.

doi: 10.1016/j.amf.2024.200157

11. Singh S, Sharma SK, Rathod DW. A review on process planning strategies and challenges of WAAM. *Mater Today Proceed*. 2021;47:6564-6575.

doi: 10.1016/j.matpr.2021.02.632

12. Dai F, Zhang S, Li R, Zhang H. Multiaxis wire and arc additive manufacturing for overhangs based on conical substrates. *Rapid Prototy J*. 2022;28(1):126-142.

doi: 10.1108/RPJ-12-2020-0300

13. Sarıkaya M, Başcıl Önler D, Dağlı S, Hartomacıoğlu S, Günay M, Królczyk GM. A review on aluminum alloys produced by wire arc additive manufacturing (WAAM): Applications, benefits, challenges and future trends. *J Mater Res Technol*. 2024;33:5643-5670.

doi: 10.1016/j.jmrt.2024.10.212

14. Tan C, Weng F, Sui S, Chew Y, Bi G. Progress and perspectives in laser additive manufacturing of key aeroengine materials. *Int J Machine Tools Manuf*. 2021;170:103804.

doi: 10.1016/j.ijmachtools.2021.103804

15. Bai JY, Yang CL, Lin SB, Dong BL, Fan CL. Mechanical properties of 2219-Al components produced by additive manufacturing with TIG. *Int J Adv Manuf Technol*. 2016;86(1):479-485.

doi: 10.1007/s00170-015-8168-x

16. Gu J, Ding J, Williams SW, Gu H, Ma P, Zhai Y. The effect of inter-layer cold working and post-deposition heat treatment on porosity in additively manufactured aluminum alloys. *J Mater Process Technol*. 2016;230:26-34.

doi: 10.1016/j.jmatprotec.2015.11.006

17. Wang Z, Xufei L, Xin L, *et al*. Porosity control and properties improvement of Al-Cu alloys via solidification condition optimisation in wire and arc additive manufacturing. *Virtual Phys Prototyp*. 2024;19(1):e2414408.

doi: 10.1080/17452759.2024.2414408

18. Pardal G, Martina F, Williams S. Laser stabilization of GMAW additive manufacturing of Ti-6Al-4V components. *J Mater Process Technol*. 2019;272:1-8.

doi: 10.1016/j.jmatprotec.2019.04.036

19. Li R, Wang R, Zhou X, *et al*. Microstructure and mechanical properties of 2319 aluminum alloy deposited by laser and cold metal transfer hybrid additive manufacturing. *J Mater Res Technol*. 2023;26:6342-6355.

doi: 10.1016/j.jmrt.2023.08.312

20. Yu A, Pan Y, Wan F, Sun G, Zhang J, Lu X. Rapid accomplishment of cost-effective and macro-defect-free LPBF-processed Ti parts based on deep data augmentation. *J Manuf Process*. 2024;120:1023-1034.

doi: 10.1016/j.jmapro.2024.05.003

21. Zhu D, Zhu H, Liu X, *et al*. CREDO: Efficient and privacy-preserving multi-level medical pre-diagnosis based on ML-KNN. *Inform Sci*. 2020;514:244-262.

doi: 10.1016/j.ins.2019.11.041

22. Headley CV, Herrera Del Valle RJ, Ma J, *et al*. The development of an augmented machine learning approach for the additive manufacturing of thermoelectric materials. *J Manuf Process*. 2024;116:165-175.

doi: 10.1016/j.jmapro.2024.02.045

23. Phua A, Cook PS, Davies CHJ, Delaney GW. Smart recoating: A digital twin framework for optimisation and control of powder spreading in metal additive manufacturing. *J Manuf Process*. 2023;99:382-391.

doi: 10.1016/j.jmapro.2023.04.062

24. Kwak J, Lee Y, Choi M, Lee S. Deep learning based approaches to enhance energy efficiency in autonomous driving systems. *Energy*. 2024;307:132625.

doi: 10.1016/j.energy.2024.132625

25. Delhaes JM, Vieira ACL, Oliveira MD. Natural language processing for participatory corporate foresight: The participant input analyzer for identifying biases and fallacies. *Technol Forecast Soc Change*. 2024;209:123652.

doi: 10.1016/j.techfore.2024.123652

26. Ling HB, Huang D, Cui J, Wang CD. HOLT-Net: Detecting smokers via human-object interaction with lite transformer network. *Eng Appl Artif Intell*. 2023;126:106919.

doi: 10.1016/j.engappai.2023.106919

27. Le-Hong T, Lin PC, Chen JZ, Pham TDQ, Van Tran X. Data-driven models for predictions of geometric characteristics of bead fabricated by selective laser melting. *J Intell Manuf*. 2023;34(3):1241-1257.

doi: 10.1007/s10845-021-01845-5

28. Zhu X, Jiang F, Guo C, Wang Z, Dong T, Li H. Prediction of melt pool shape in additive manufacturing based on machine learning methods. *Optics Laser Technol*. 2023;159:108964.

doi: 10.1016/j.optlastec.2022.108964

29. Liu S, Brice C, Zhang X. Interrelated process-geometry-microstructure relationships for wire-feed laser additive manufacturing. *Mater Today Commun*. 2022;31:103794.

doi: 10.1016/j.mtcomm.2022.103794

30. Xia C, Pan Z, Polden J, Li H, Xu Y, Chen S. Modelling and prediction of surface roughness in wire arc additive manufacturing using machine learning. *J Intell Manuf*. 2022;33(5):1467-1482.

doi: 10.1007/s10845-020-01725-4

31. Oh WJ, Lee CM, Kim DH. Prediction of deposition bead geometry in wire arc additive manufacturing using machine learning. *J Mater Res Technol*. 2022;20:4283-4296.

doi: 10.1016/j.jmrt.2022.08.154

32. Šket K, Brezočnik M, Karner T, *et al*. Predictive modelling of weld bead geometry in wire arc additive manufacturing. *J Manuf Mater Process*. 2025;9(2):67.

doi: 10.3390/jmmp9020067

33. Ren Y, Zhang L, Suganthan PN. Ensemble classification and regression-recent developments, applications and future directions [review article]. *IEEE Comput Intell Mag*. 2016;11(1):41-53.

doi: 10.1109/MCI.2015.2471235

34. Huang W, Chen S, Xiao J, Jiang X, Jia Y. Laser wire-feed metal additive manufacturing of the al alloy. *Optics Laser Technol*. 2021;134:106627.

doi: 10.1016/j.optlastec.2020.106627

35. Shukla P, Chitral S, Kumar T, Kiran DV. The influence of GMAW correction parameters on stabilizing the deposition characteristics for wire arc additive manufacturing. *J Manuf Process*. 2023;90:54-68.

doi: 10.1016/j.jmapro.2023.01.075

36. Gong M, Zhang S, Lu Y, Wang D, Gao M. Effects of laser power on texture evolution and mechanical properties of laser-arc hybrid additive manufacturing. *Addit Manuf*. 2021;46:102201.

doi: 10.1016/j.addma.2021.102201

37. Ferreira SLC, Bruns RE, Ferreira HS, *et al*. Box-Behnken design: An alternative for the optimization of analytical methods. *Anal Chim Acta*. 2007;597(2):179-186.

doi: 10.1016/j.aca.2007.07.011

38. Fang X, Ren C, Zhang L, Wang C, Huang K, Lu B. A model of bead size based on the dynamic response of CMT-based wire and arc additive manufacturing process parameters. *Rapid Prototy J*. 2021;27(4):741-753.

doi: 10.1108/RPJ-03-2020-0051

39. Brown CE. Coefficient of variation. In: Brown CE, editor. *Applied Multivariate Statistics in Geohydrology and Related Sciences*. Berlin: Springer Berlin Heidelberg; 1998. p. 155-157.

doi: 10.1007/978-3-642-80328-4

40. Burdick RK, Borror CM, Montgomery DC. A review of methods for measurement systems capability analysis. *J Q Technol*. 2003;35(4):342-354.

doi: 10.1080/00224065.2003.11980232

41. Kennedy J, Eberhart R. *Particle Swarm Optimization*. Vol. 4. United States: IEEE; 1995. p. 1942-1948.

doi: 10.1109/ICNN.1995.488968

42. Huang GB, Zhu QY, Siew CK. Extreme learning machine: Theory and applications. *Neurocomputing*. 2006;70(1): 489-501.

doi: 10.1016/j.neucom.2005.12.126

43. Awad M, Khanna R. Support vector regression. In: Awad M, Khanna R, editors. *Efficient Learning Machines: Theories, Concepts, and Applications for Engineers and System Designers*. New York: Apress; 2015. p. 67-80.

doi: 10.1007/978-1-4302-5990-9

44. Schulz E, Speekenbrink M, Krause A. A tutorial on Gaussian

process regression: Modelling, exploring, and exploiting functions. *J Math Psychol*. 2018;85:1-16.

doi: 10.1016/j.jmp.2018.03.001

45. Shapley LS. Quota solutions of n-person games. In: Harold William K, Albert William T, editors. *Contributions to the Theory of Games*. Vol. 2. United States: Princeton University Press; 1953. p. 343-360.

46. Liu CA, Kuo BS. Model averaging in predictive regressions. *Econom J*. 2016;19(2):203-231.

doi: 10.1111/ectj.12063

47. Mu G, Wei Q, Xu Y, Zhang H, Zhang J, Li Q. Capacity estimation for lithium-ion batteries based on heterogeneous stacking model with feature fusion. *Energy*. 2024;313:133881.

doi: 10.1016/j.energy.2024.133881

48. Wang R, Cheng MN, Loh YM, Wang C, Fai Cheung C. Ensemble learning with a genetic algorithm for surface roughness prediction in multi-jet polishing. *Exp Syst Appl*. 2022;207:118024.

doi: 10.1016/j.eswa.2022.118024

49. Chung J, Shen B, Kong ZJ. Anomaly detection in additive manufacturing processes using supervised classification with imbalanced sensor data based on generative adversarial network. *J Intell Manuf*. 2024;35(5):2387-2406.

doi: 10.1007/s10845-023-02163-8

50. Chua C, Liu Y, Williams RJ, Chua CK, Sing SL. In-process and post-process strategies for part quality assessment in metal powder bed fusion: A review. *J Manuf Syst*. 2024;73:75-105.

doi: 10.1016/j.jmsy.2024.01.004